

# We are IntechOpen, the world's leading publisher of Open Access books Built by scientists, for scientists

6,900

Open access books available

185,000

International authors and editors

200M

Downloads

Our authors are among the

154

Countries delivered to

TOP 1%

most cited scientists

12.2%

Contributors from top 500 universities



WEB OF SCIENCE™

Selection of our books indexed in the Book Citation Index  
in Web of Science™ Core Collection (BKCI)

Interested in publishing with us?  
Contact [book.department@intechopen.com](mailto:book.department@intechopen.com)

Numbers displayed above are based on latest data collected.  
For more information visit [www.intechopen.com](http://www.intechopen.com)



# Aviation Applications of Doppler Radars in the Alerting of Windshear and Turbulence

P.W. Chan<sup>1</sup> and Pengfei Zhang<sup>2</sup>

<sup>1</sup>*Hong Kong Observatory, Hong Kong,*

<sup>2</sup>*University of Oklahoma, Norman, OK,*

<sup>1</sup>*China*

<sup>2</sup>*USA*

## 1. Introduction

Doppler radars are indispensable nowadays in the assurance of aviation safety. In particular, many airports in the world are equipped with Terminal Doppler Weather Radar (TDWR) in the alerting of low-level windshear and turbulence. The microburst alerts from certain TDWR are taken as “sky truth” and the aircraft may not fly when microburst alerts are in force.

This chapter summarizes some recent developments on the aviation applications of TDWR in Hong Kong (Figure 1). It first starts with a case study of a typical event of microburst alert associated with severe thunderstorms. The applications of TDWR in the alerting of windshear and turbulence are then described, namely, in the calculation of windshear hazard factor using the radial velocity data from the radar, and the calculation of eddy dissipation rate based on the spectrum width data of the radar. It is hoped that this chapter could serve as an introduction to the aviation applications of TDWR, for the reference of the weather services of other airports.

## 2. A typical microburst event leading to missed approaches of aircraft

The missed approaches at the Hong Kong International Airport (HKIA) took place during the overnight period of 8 to 9 September 2010 when intense thunderstorm activity brought heavy rain and frequent lightning to the whole Hong Kong. During the period, an intense rain band with north-south orientation swept from east to west across Hong Kong. More than 50 millimeters of rainfall in an hour were generally recorded over the territory and a record-breaking number of 13,102 cloud-to-ground lightning strokes were registered during the hour just after midnight. When the thunderstorms edged close to the HKIA which is situated at the western part of the territory, gusty strong easterlies from the downdraft of the thunderstorm first affected the flight paths east of the airport resulting in an abrupt change in the prevailing winds from southwesterlies to easterlies.

Two flights, which tried to land as the thunderstorms approached HKIA, aborted landing and diverted to Macao eventually. Both flights approached the HKIA from the east under the prevailing southwesterly winds (Figure 2). The first aircraft went around twice. The first



Fig. 1. The locations of the Hong Kong TDWR (red dot) radar and Hong Kong International Airport (HKIA). The blue beams illustrate the radar beams over the runways corridor 07LA of the airport with 1° azimuth interval. Three yellow lines indicate the approach paths and their names are marked.

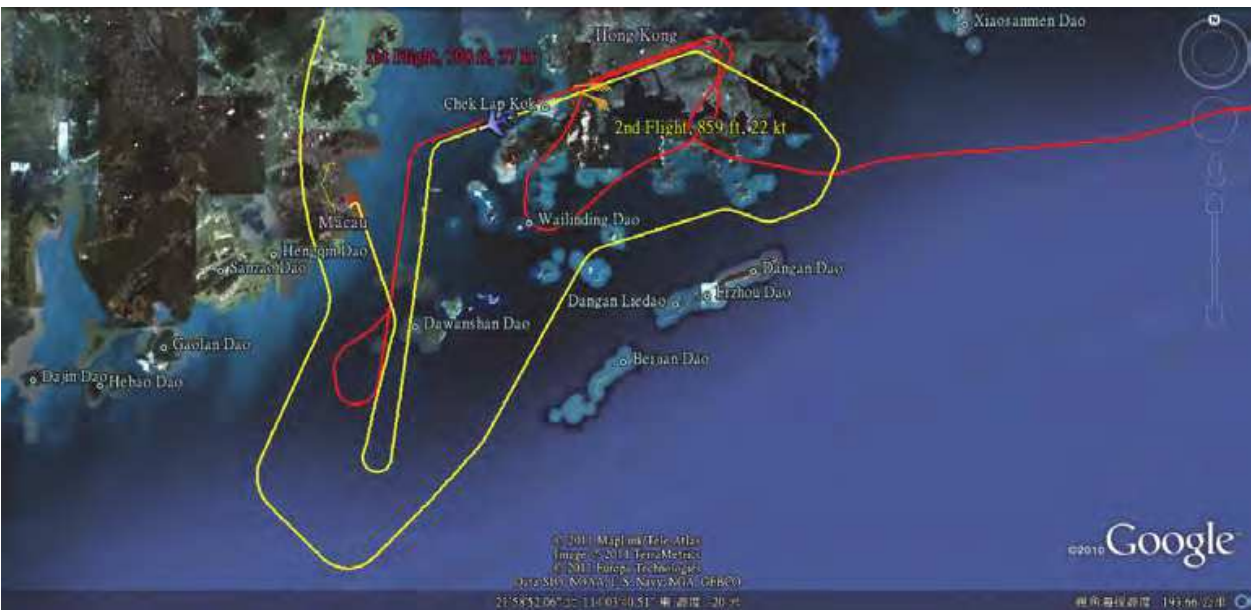


Fig. 2. Flight paths of the two aircraft which had to conduct missed approach. Red line indicated the flight path for the first aircraft and yellow for the second aircraft. Orange wind barbs showed the locations of aircraft when tailwind was encountered. The 1<sup>st</sup> and 2<sup>nd</sup> aircraft recorded tailwind of 37 and 22 knots respectively.

aborted landing was due to technical consideration. In the second approach at around 00:08 HKT (=UTC + 8 hours), it encountered strong tailwind. Landing was subsequently aborted and the aircraft diverted to Macao thereafter. Four minutes later, the second aircraft followed the same glide path of the first aircraft but also failed to land at the HKIA because of the same reason, i.e. the strong tailwind. The aircraft was also diverted to Macao at 00:12 HKT.

Flight data retrieved from the flight data recorders of the two aircraft was analyzed to reveal the meteorological conditions encountered by aircrafts. It appeared that the missed approach was attributable to the strong tailwind which exceeded the airline pre-defined threshold, namely 15 knots for tailwind landing.

According to the flight data, the first aircraft experienced more than 15 knots tailwind after it descended to below 1600 feet (Figure 3(a)) in its second approach. The tailwind increased from 25 knots when the aircraft descended to 780 feet (labeled 'A' in Figure 3(a)) and strengthened to 37 knots at 708 feet at 00:08 HKT (labeled 'B' in Figure 3(a)), which far exceed the limit for tailwind landing. As a result, diversion to other airport was conducted.

The second aircraft also experienced the tailwind of around 15 knots when it descended to around 1600 feet. The tailwind increased and reached 19 knots when the aircraft descended to 1423 feet (labeled 'C' in Figure 3(b)) but then decreased and fluctuated between 7 to 12 knots when the aircraft further descended to 1028 feet (labeled 'D' in Figure 3(b)). At around 00:12 HKT, the tailwind started to strengthen again and exceeded 15 knots. The maximum tailwind experienced by the aircraft was 22 knots, which also exceeded the limit for tailwind landing, at 859 feet above the runway (labeled 'E' in Figure 3(b)). Similar to the first aircraft, the second aircraft executed a missed approach due to the strong tailwind and was diverted to Macao.

The TDWR also captured the wind conditions when the two aircraft conducted missed approaches. Figures 4(a) and 4(b) showed the radial velocity measured by TDWR at 0008 HKT and 0012 HKT 9 September respectively. Gusts reaching 27 m/s (i.e. around 50 knots) were captured by the TDWR over the eastern part of the HKIA. The zero isotach, which marked the leading edge of the shear line, agreed well with that identified based on anemometer data.

The HKO Windshear and Turbulence Alerting System (WTWS) integrates windshear and turbulence alerts generated by different algorithms such as Anemometer-based Windshear Alerting Rules-Enhanced (AWARE) (Lee, 2004), LIDAR Windshear Alerting System (LIWAS) (Shun and Chan, 2008), TDWR alerts and other algorithms. Alerts are then generated for 8 runway corridors (north runway and south runway have two arrival and two departure corridors each) and shown on a graphical display, the WTWS display.

At 0008 HKT, the zero isotach over the HKIA detected by the TDWR was analyzed as a gust front and was shown on the WTWS display (Figure 5(a)). In addition, microburst alerts, which represent windshear loss of 30 knots or more with precipitation, were provided by TDWR to the east of the HKIA; windshear alerts were generated from AWARE over the runways; turbulence alerts were in force due to the thunderstorm to the north of the HKIA. Over the 8 corridors of the HKIA, all had windshear alerts with magnitude ranging from +25 to +30 knots. At 0012 HKT, although the gust front was not detected by the TDWR



(Figure 5(b)) any more, using the surface anemometers and TDWR base data, windshear alerts with magnitude ranging from +15 to +25 knots were issued for the four western corridors. Meanwhile, areas with the microburst alerts shifted westwards and affected the eastern corridors. WTWS issued microburst alerts of -35 knots to the four eastern corridors. During the event, the WTWS functioned properly and was able to provide adequate warning to the aircraft of the windshear to be expected due to the thundery weather.

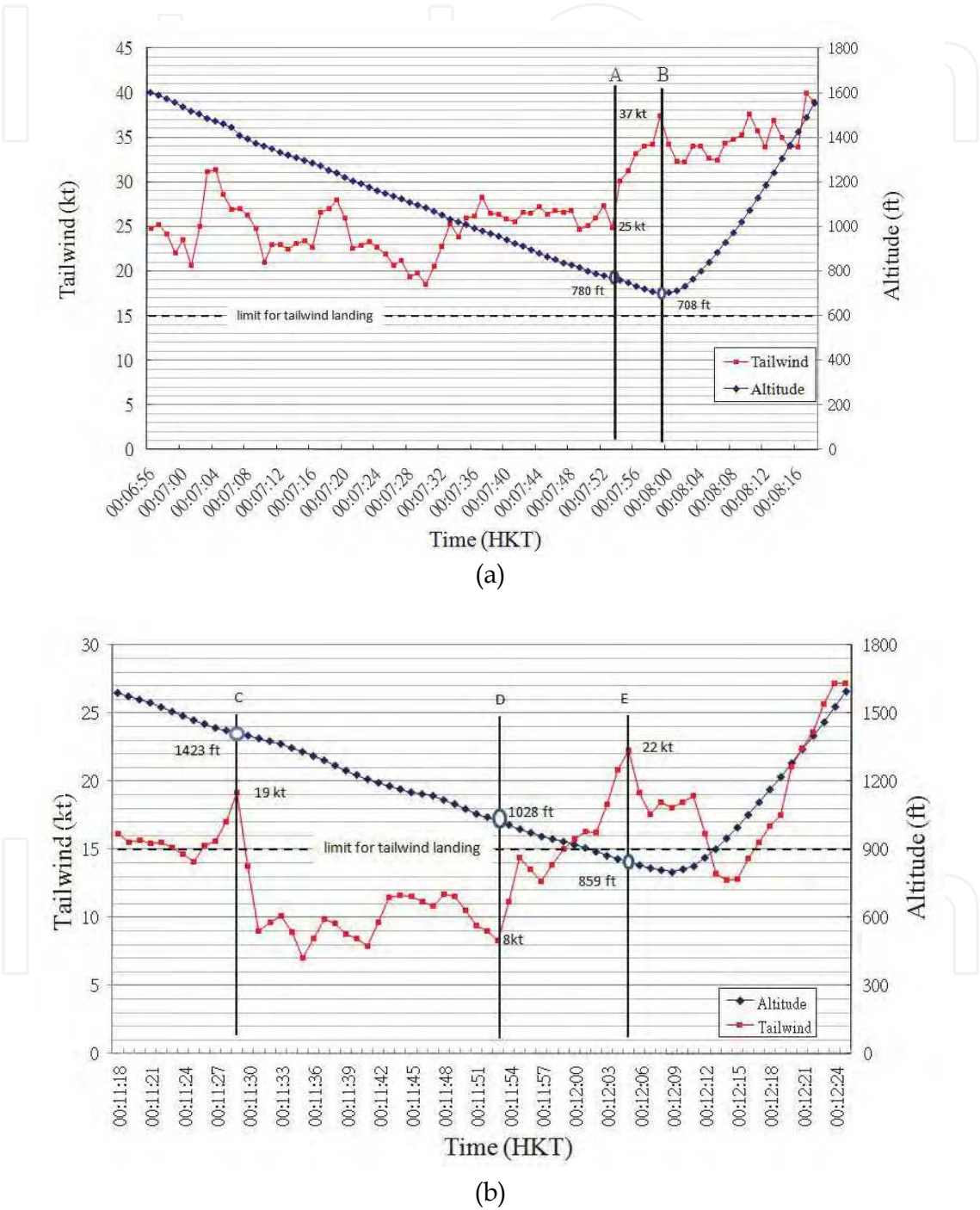


Fig. 3. Time series in HKT of tailwind in knots (red square) and aircraft altitude in feet (blue diamond) retrieved from the flight data recorders. (a) Flight data for the first aircraft. Tailwind reached 37 knots at 00:08 HKT. (b) Flight data for the second aircraft.

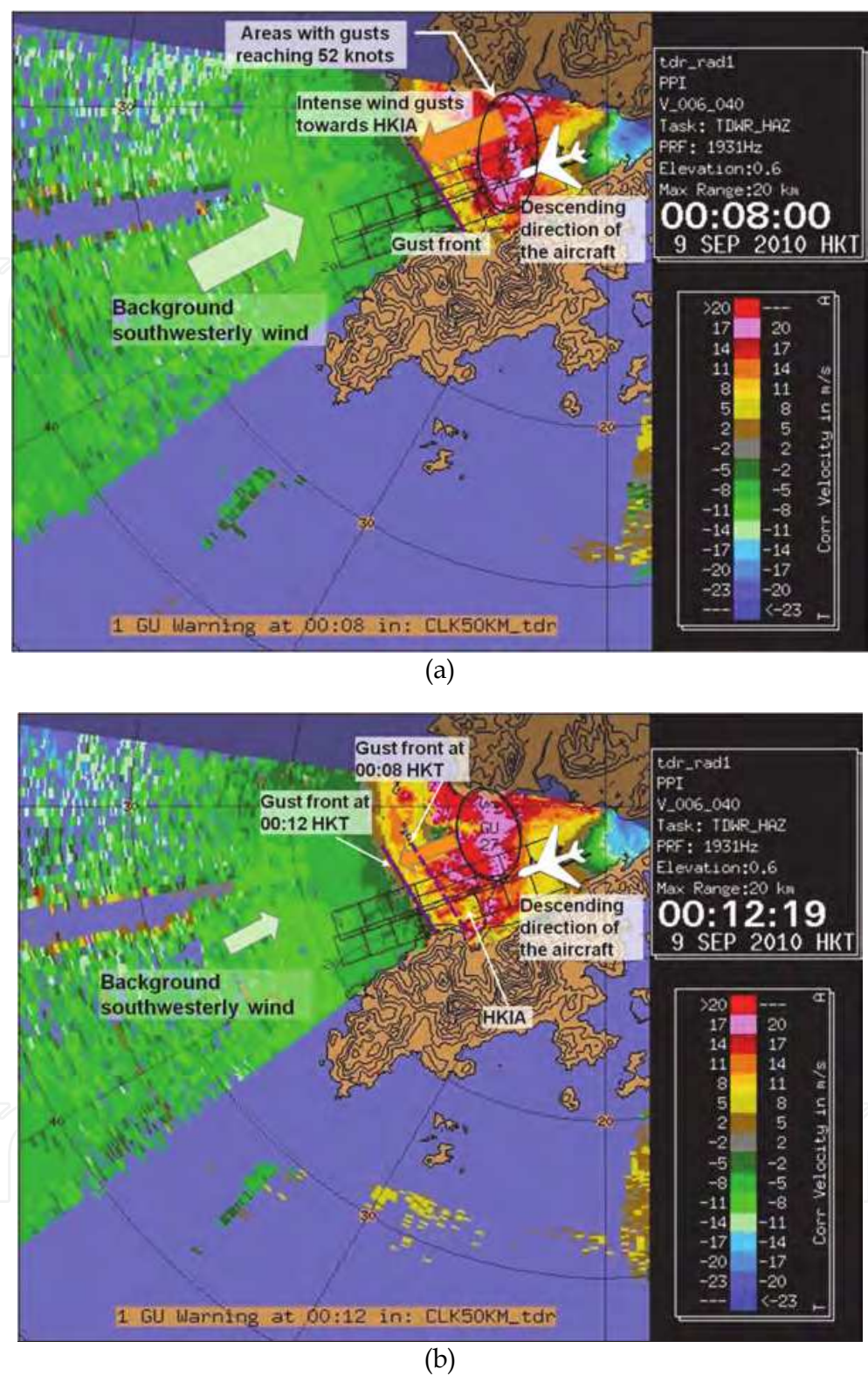
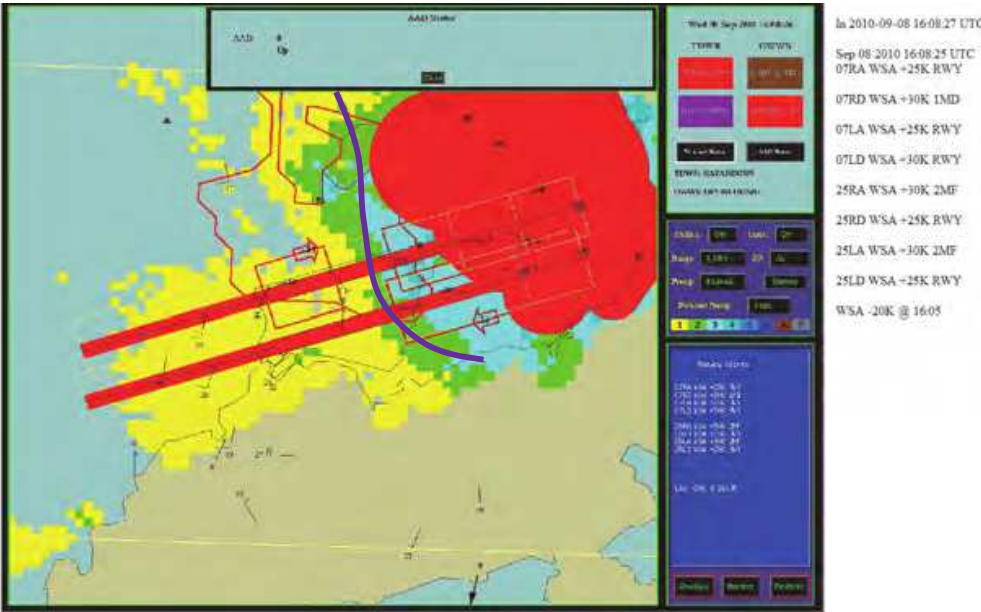
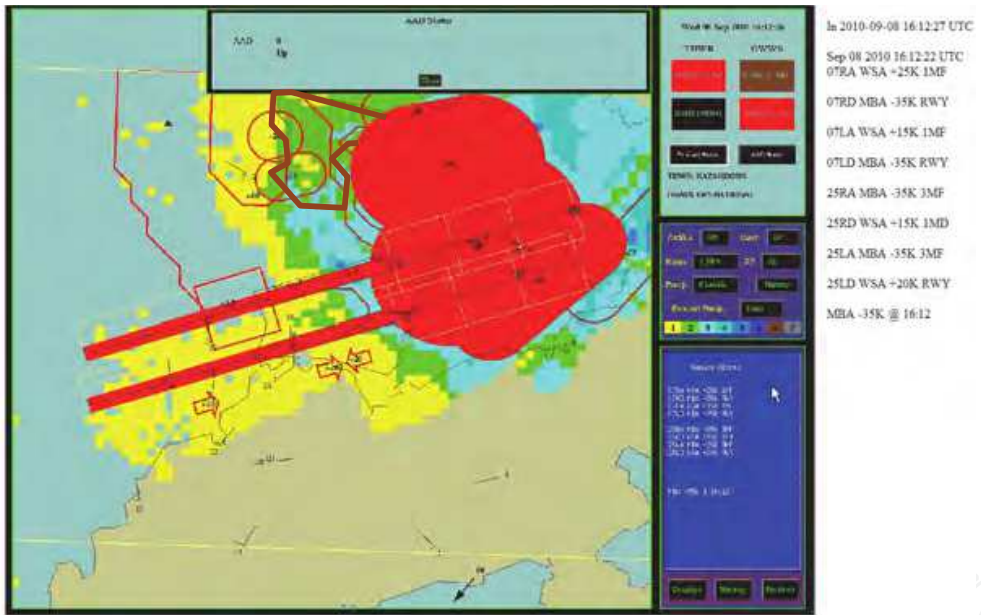


Fig. 4. Velocity measured by TDWR on 9 September 2010. The cool/warm colors represent winds towards/away from the TDWR. Area with gusts reaching 27 m/s was circled in black. The zero isotach (gust front) was in purple. (a) TDWR image at 0008 HKT; (b) TDWR images at 0012 HKT. The zero isotach (gust front) moved westwards to the western end of HKIA.





(a)



(b)

Fig. 5. WTWS display on 9 September 2010. Gust front analyzed by TDWR (purple line) over the HKIA; microburst alerts generated by TDWR (red solid band-aids); windshear alerts generated by AWARE (red hollow rectangles), by TDWR (red hollow irregular polygons); by LIDAR (red arrows, over the runways only); turbulence alert generated by TDWR (brown polygon with dots). Black numbers were the windshear magnitude in knots. (a) 0008 HKT on 9 September 2010. A gust front was over the HKIA. Windshear alerts were issued by the WTWS for all runway corridors. LIDAR data was highly attenuated by precipitation and could only detect windshear over the runway. (b) 0012 HKT on 9 September 2010. Microburst alerts of -35 knots were issued to the four eastern corridors. Windshear alerts with magnitude ranging from +15 to +25 knots were issued for the four western corridors.

### 3. Windshsear hazard factor based on TDWR

In aviation meteorology, windshear refers to a sustained change of wind speed and/or wind direction that causes the aircraft to deviate from the intended flight path. Low-level windshear (below 1600 feet) could be hazardous to the arriving/departing aircraft. Hong Kong is situated in a subtropical coastal area and it is common to have intense convective weather in the spring and summer. To alert low-level windshear associated with microburst and gust front, a TDWR is operated by the Hong Kong Observatory (HKO) in the vicinity of HKIA (Figure 1). It is a C-band radar with 0.5-degree half-power beam width scanning over the airport and determines convergence/divergence features along the runway orientation from the Doppler velocities. Windshear alerts are generated when the velocity change is 15 knots or more.

Another index that quantifies the windshear threat is the F-factor (Proctor et al., 2000). It is based on the fundamentals of flight mechanics and the understanding of windshear phenomena. The F-factor could also be calculated from the Quick Access Recorder (QAR) data recorded on the commercial jets (Haverdings, 2000). In this study, an attempt is made to calculate F-factor for some typical microburst events at HKIA based on the TDWR measurements and the results are compared with the F-factor determined from the QAR data.

F-factor is calculated from TDWR's radial velocity data in two steps. First of all, convergence/divergence features are identified from the TDWR data. Then F-factor is determined from each convergence/divergence feature by assuming a wind field model of microburst. The two steps are briefly described below.

To compute convergence/divergence features, the method described in Merritt (1987) is adopted. The TDWR microburst detection algorithm identifies microburst by searching for significant velocity difference along a radial in a search window of 4 range gates ( $4 \times 150$  metres per gate = 600 metres in length, and one degree in azimuth). If the windshear along a search window is divergent (i.e. radial wind generally increases with increasing distance from the radar), the search window is taken to be a divergence shear segment. Likewise, convergence shear segment is also identified.

Two divergence/convergence segments are associated as a divergence/convergence shear features if their minimum overlap in range is 0.5 km or if their maximum angular spacing is 2 degrees azimuth. A divergence/convergence region contains at least 4 shear segments with a minimum length of 0.95 km and a minimum area of 1 km<sup>2</sup>. Moreover, the maximum velocity difference among the shear segments inside a divergence region should be at least 5 m/s. As such, the shear within a divergence region is at least 5 m/s per 600 m, i.e. 0.008 m/s/m.

F-factor is related to the total aircraft energy and its rate of change, and is defined to be:

$$F = \frac{\dot{W}_x}{g} - \frac{w}{V_a} \quad (1)$$

where  $W_x$  is the component of atmospheric wind directed horizontally along the flight path (direction  $x$ ) and  $\dot{W}_x$  its rate of change,  $g$  the acceleration due to gravity,  $w$  the updraft of



the atmosphere, and  $V_a$  the airspeed of the aircraft. By estimating the updraft from mass continuity constraint, it is shown to be equivalent to:

$$F = \frac{\partial W_x}{\partial x} \left[ \frac{V_g}{g} + \frac{2h}{V_a} \right] \quad (2)$$

where  $V_g$  is the ground speed of the aircraft, and  $h$  the altitude above ground.

For each convergence/divergence feature captured by the TDWR, the velocity change  $\Delta U$  and the distance over which this change occurs  $\Delta R$  are calculated. It is shown in Hinton (1993) with reference to a microburst model that F-factor could be calculated from:

$$F = K \frac{\Delta U}{\Delta R} \left[ \left( \frac{\Delta R}{L} \right)^2 - \left( \frac{\Delta R}{L} \right)^3 \frac{\sqrt{\pi}}{2\alpha} \operatorname{erf} \left( \frac{\alpha L}{\Delta R} \right) \right] \bullet \left[ \frac{V_g}{g} + \frac{2h_r}{V_a} \right] \quad (3)$$

where  $K = 4.1925$ ,  $a = 1.1212$ ,  $h_r$  the above-ground-level (AGL) altitude of the TDWR radar beam,  $L$  the characteristic shear length of 1000 m, and  $\operatorname{erf}(y)$  the error function.

The microburst model in Hinton (1993) includes a shaping function which describes the change in microburst outflow with altitude. This function is given by:

$$p(h) = \frac{e^{-0.22h/H} - e^{-2.75h/H}}{0.7386} \quad (4)$$

where  $h$  is the altitude above ground and  $H$  the altitude of maximum outflow speed (assumed to be 90 m). The F-factor  $F_1$  from the TDWR at the radar beam altitude  $h_1$  is then related to the F-factor  $F_2$  of the aircraft at the altitude  $h_2$  by the following equation:

$$F_2 = F_1 \frac{p(h_2) \left( \frac{V_g}{g} + \frac{2h_2}{V_a} \right)}{p(h_1) \left( \frac{V_g}{g} + \frac{2h_1}{V_a} \right)} \quad (5)$$

Combining (3) – (5) and with  $\Delta U$  and  $\Delta R$  determined, the F-factor associated with a divergence/convergence feature at the altitude of the aircraft along the glide path could be calculated.

For the formulation in (1), F-factor is positive if the windshear is performance decreasing (headwind decreasing or downdraft) and negative if the windshear is performance increasing (headwind increasing or updraft). As discussed in Proctor et al. (2000), for onboard windshear systems, the windshear is considered to be hazardous if  $F$  is greater than 0.1, and a *must alert* threshold is set to be 0.13. The must alert threshold means a wind shear alert must be issued when that threshold is reached/exceeded.

A microburst event that affected HKIA on 18 May 2007 is considered here as an illustration of the method. In the evening of that day, a surface trough of low pressure lingered around the south China coast, bringing unsettled weather to the region. Between 09 and 10 UTC (5 and 6 p.m. of 18 May 2007), a band of strong radar echoes with east-northeast to west-

southwest orientation moved southeastwards from inland areas across the coast. At HKIA, the TDWR issued microburst alerts of 30 knots headwind loss for the aircraft between 09:20 and 09:27 UTC.

Figure 6(a) shows the moment when a microburst associated with the thunderstorms affected the runway corridors to the east of HKIA. Divergent flow feature was found at 0.6-degree conical scan of TDWR. For an aircraft arriving at the north runway of HKIA (location in Figure 1) from the east, the windshear associated with the microburst is performance decreasing (due to decreasing headwind). Using the formulae above, the F-factor for the microburst is determined to be about 0.14, which exceeds the must alert threshold and the windshear associated with the microburst is considered to be hazardous to the aircraft. Flight data are obtained for an aircraft arriving at the north runway from the east at that time. They are processed by the algorithm in Haverdings (2000) and the variation of F-factor along the glide path is shown in Figure 6(b). At about the location of the microburst (near the eastern threshold of the north runway), the F-factor is found to be about 0.13, which is generally consistent with the value determined from TDWR data. Thus for microburst associated with the thunderstorm, the F-factor determined from TDWR measurements and that from QAR data of the aircraft are comparable with each other. The other peaks/troughs of F-factor from the QAR data (Figure 6(b)) are not revealed in the TDWR measurements. They may not be properly handled by the microburst model for F-factor calculation.

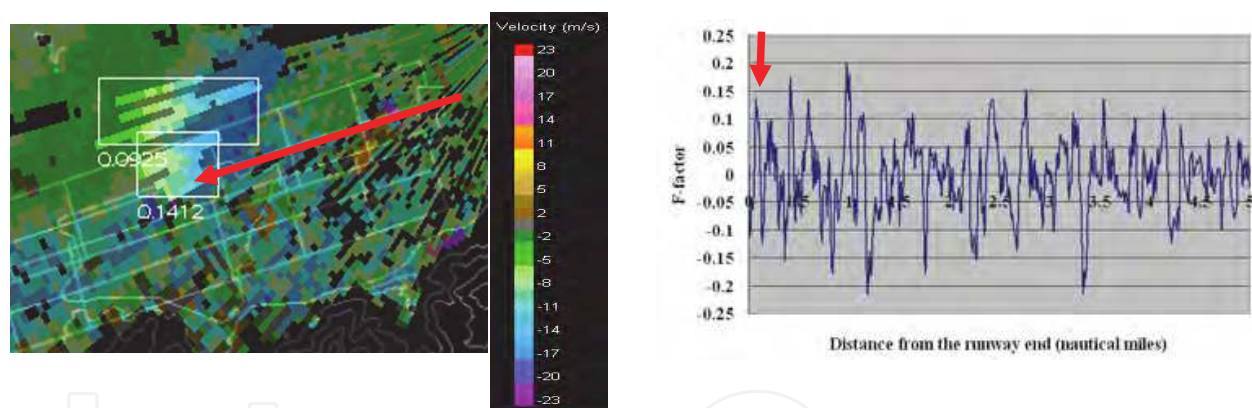


Fig. 6. (a) Divergence features (highlighted in lighter colours) associated with microburst on 18 May 2007, overlaid on the radial velocity from the TDWR (colour scale on the right). F-factor of each feature is given as a number next to the box indicating the location of the feature. (b) F-factor as recorded on an aircraft flying at about the same time as in (a) along the glide path shown as a red arrow in (a). The red arrow in (b) is the approximate location of the windshear feature encountered by the aircraft.

To study the change in the F-factor following the evolution of the microburst, the intense convective event on 8 June 2007 is considered. Severe gusts associated with thunderstorms and microburst with a recorded maximum of 35.9 m/s affected HKIA in the morning of that day. A helicopter parked on the apron toppled in strong winds during the passage of the intense storm cells. We just focus on the windshear hazard associated with the microburst. The divergence features determined from the radial velocity of the TDWR at 0.6-degree conical scans are shown in Figure 7. Stronger winds associated with the microburst got

closer to the ground level (about 260 m above mean sea level at the location of the microburst) in a short time interval within 3 minutes, with the maximum value of towards-the-radar velocity increasing from 18 m/s (dark blue in Figure 7) to 23 m/s (magenta in Figure 7). As a result, the F-factor increases in magnitude from 0.14 to 0.23, which exceeds the must alert threshold. The TDWR-based F-factor provides a good indication about the level of hazard associated with an evolving microburst.

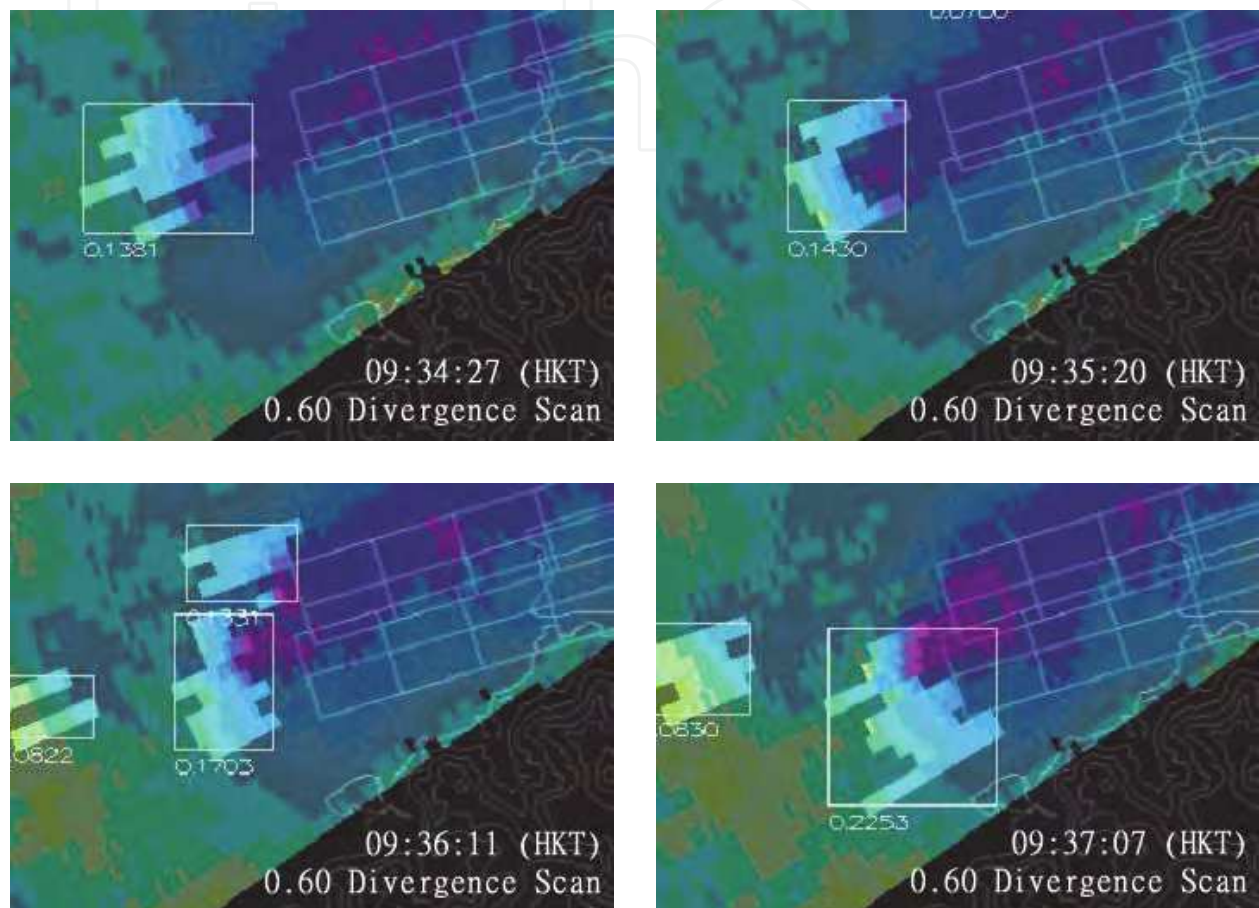


Fig. 7. Time series of the divergence feature associated with a microburst on 8 June 2007. The feature is highlighted in lighter colour and enclosed in a box. The number next to the box is the F-factor calculated for the feature. The background is the radial velocity from the TDWR, with the colour scale given in Figure 6.

Besides intense convective weather, the windshear hazard in terrain-disrupted airflow is also studied. The Typhoon Prapiroon case on 3 August 2006 is considered. On that day, Prapiroon was located at about 200 km to the southwest of Hong Kong over the South China Sea and tracked northwest towards the western coast of southern China. This typhoon brought about gale-force east to southeasterly airflow to Hong Kong. Due to complex terrain to the south of the airport, airflow disturbances occurred inside and around HKIA. Divergent flow features were observed near the airport from time to time. Figure 8(a) shows such a feature at 0.6-degree conical scan of the TDWR at about 4:47 a.m., 3 August. The F-factor associated with this feature is about 0.22, which exceeds the must alert threshold for windshear. An aircraft landed at the north runway of HKIA from the west at about that time (within one minute). The variation of the F-factor determined from QAR



data along the glide path is given in Figure 8(b). At the location of the microburst, the F-factor from the aircraft is comparable with that calculated from the TDWR data, even for this case of terrain-disrupted airflow. As discussed in the first case study, the other peaks/troughs of F-factor from the QAR data (Figure 8(b)) are not revealed in the TDWR measurements. They may not be properly handled by the microburst model for F-factor calculation.

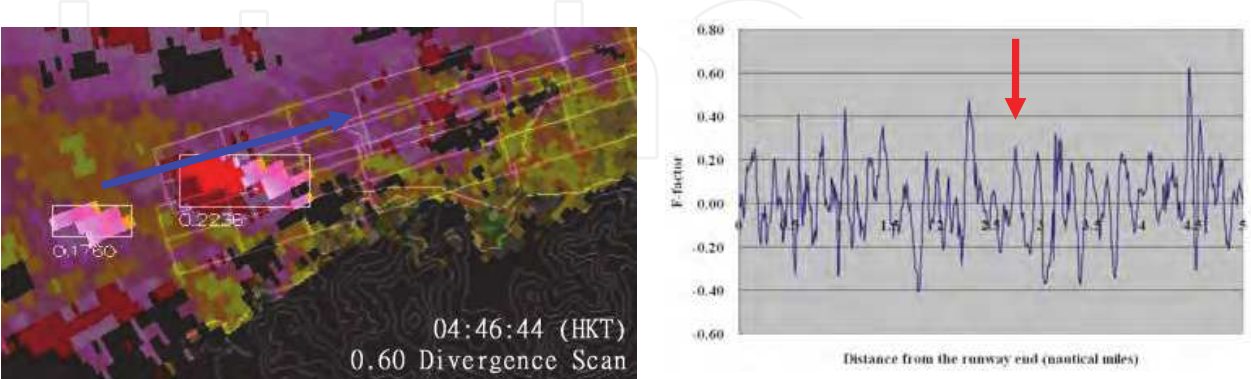


Fig. 8. (a) Divergence features (highlighted in lighter colours) associated with windshear in terrain-disrupted airflow on 3 August 2006, overlaid on the radial velocity from the TDWR (colour scale given in Figure 6). F-factor of each feature is given as a number next to the box indicating the location of the feature. (b) F-factor as recorded on an aircraft flying at about the same time as in (a) along the glide path shown as a blue arrow in (a). The red arrow in (b) is the approximate location of the windshear feature encountered by the aircraft.

4. Calculation of turbulence intensity

The measurement of spectrum width is determined not only by the Doppler velocity distribution and density distribution of the scatterers within the resolution volume, but also radar observation parameters like beamwidth, pulse width, antenna rotation rate, etc. According to Doviak and Zrnic (2006), there are five major spectral broadening mechanisms that contribute to the spectrum width measurements, which can be written as follow

$$\sigma_v^2 = \sigma_s^2 + \sigma_t^2 + \sigma_\alpha^2 + \sigma_d^2 + \sigma_o^2$$
 (6)

where  $\sigma_s$  represents mean wind shear contribution,  $\sigma_t$  represents turbulence,  $\sigma_\alpha$  represents antenna motion,  $\sigma_d$  represents different terminal velocities of hydrometeors of different sizes, and  $\sigma_o$  represents variations of orientations and vibrations of hydrometeors. Except  $\sigma_s$  and  $\sigma_t$  the rest of the terms on the right hand side of the Eq.(6) are considered to be negligible for the measurements of  $\sigma_v$  in this paper (Brewster and Zrnic, 1986). Thus the turbulence term  $\sigma_s$  can be obtained,

$$\sigma_t^2 = \sigma_v^2 - \sigma_s^2.$$
 (7)

In the Eq.(7), mean wind shear width term  $\sigma_s$  can be decomposed into three terms due to mean radial velocity shear at three orthogonal directions in radar coordinate(Doviak and Zrnic, 2006):

$$\sigma_s^2 = \sigma_{s\theta}^2 + \sigma_{s\phi}^2 + \sigma_{sr}^2 = (r_0\sigma_\theta k_\theta)^2 + (r_0\sigma_\phi k_\phi)^2 + (\sigma_r k_r)^2, \quad (8)$$

where  $\sigma_r^2 = (0.35c\tau/2)^2$ ,  $\sigma_\theta^2 = \theta_1^2/16\ln 2$ , and  $\sigma_\phi^2 = \theta_1^2/16\ln 2$ . Here  $c\tau/2$  is range resolution, and  $\theta_1$  is the one-way angular resolution (i.e., beamwidth).  $k_\theta$ ,  $k_\phi$ , and  $k_r$  are the components of shear along the three orthogonal directions.

In order to use  $\sigma_t$  to estimate eddy dissipation rate (EDR)  $\varepsilon$ , it must be assumed that within radar resolution volume turbulence is isotropic and its outer scale is larger than the maximum dimension of the radar's resolution volume (which is indicated as  $V_0$ ). Under these assumptions, in the case of  $\sigma_r \leq r\sigma_\theta$  the relation between turbulence spectrum width  $\sigma_t$  and EDR  $\varepsilon$  can be approximately written as (Labitt, 1981)

$$\varepsilon \approx \frac{0.72\sigma_t^3}{r\sigma_\theta A^{3/2}}, \quad (9)$$

where  $A$  is constant (i.e., about 1.6). When  $\sigma_r \geq r\sigma_\theta$ , the relation can be approximated by

$$\varepsilon \approx \left[ \frac{\langle \sigma_t^2 \rangle^{3/2}}{\sigma_r (1.35A)^{3/2}} \right] \left( \frac{11}{15} + \frac{4}{15} \frac{r^2 \sigma_\theta^2}{\sigma_r^2} \right)^{-3/2} \quad (10)$$

Eqs. (9) and (10) are used to estimate EDR using Hong Kong TDWR observed spectrum width.

In hazardous weather mode, the Hong Kong TDWR conducts sector scans from azimuth  $182^\circ$  to  $282^\circ$  (i.e., confined to the approach and departure paths). Each sector scan takes about 4 minutes. Thus, the low altitude wind shear can be detected within a minute. The range and angular resolutions of the radar are 150 m and  $0.5^\circ$  respectively. The maximum range reaches 90 km. The radar data includes reflectivity, Doppler velocity, spectrum width, and signal-to-noise ratio (SNR) recorded with the azimuth interval of  $1^\circ$ .

Based on the Eqs. (9) and (10), EDR can be estimated when spectrum width observation is available. In this feasibility study, EDR estimation is only performed at the lowest elevation angle of  $0.6^\circ$ . The vertical wind shear contribution to the EDR is calculated by using spatially averaged mean Doppler velocity at two lowest elevation angles. Because the closest two elevation angles at lowest level are  $0.6^\circ$  and  $1.0^\circ$  at scans 11 and 12, vertical wind shear is calculated by using the Doppler velocity fields at these two scans. For simplicity, EDR is estimated at scan 17 with elevation angle of  $0.6^\circ$ . Azimuthal and radial wind shear is also calculated at this scan. So in the current algorithm, one EDR field at elevation angle of  $0.6^\circ$  will be generated for each volume scan.

The control of the TDWR spectrum width data quality is very important for EDR estimation. It has been found that there is a variety of sources of errors in spectrum width measurements in previous studies (Fang et al. 2004). Especially if signal to noise ratio (SNR) is low, spectrum width measurements have large variance. In this study,  $\text{SNR} > 20$  dB is assigned as a simple and straightforward threshold for the EDR estimates. In other words, EDR at the gate with  $\text{SNR} < 20$  dB is marked as missing data (MD) in our algorithm. In the future, more comprehensive quality control processor will be designed and implemented in our algorithm to deal with other error sources.

Following international practice, EDR values are classified into four categories in terms of the intensity of turbulence. For convenience and in line with alerting purpose of low-level turbulence, EDRs in the following figures and context will be labeled or indicated as insignificant (LL), light (L), moderate (M), and severe (S) instead of its value. It is also worth mentioning that EDR values presented in this paper are derived from the spectrum width data after smoothing by using a 9 point median filter along the radar beams in order to suppress the fluctuations in the determination of spectrum width values. This kind of fluctuation is expected, for instance, to arise from the limited and finite number of data points in the digitization of the spectrum of the return signal.

The spectrum width errors are large in region of low SNR. Here we selected a case to demonstrate the importance of the SNR threshold in the quality control of EDR data. Around 21 UTC on 6 June 2008, the TDWR radar observed thunderstorms over HKIA. Without SNR threshold, estimated EDR suggested severe turbulence region (red color; Figure 9(a)) in the region about azimuth of  $270^\circ$  and centered at about 25 km. High spectrum widths ( $\sim 4.5$  m/s) are indeed measured in this region (see Figure 9(c)). But reflectivity (Figure 9(e)) and SNR (Figure 9(d)) are around -8 dBZ and 10 dB respectively. The relatively large spectrum widths in this region can be caused by incorrect noise power estimates (Fang et al., 2004). To avoid such biases, we use a SNR threshold of 20 dB as recommended by Fang et al., (2004).

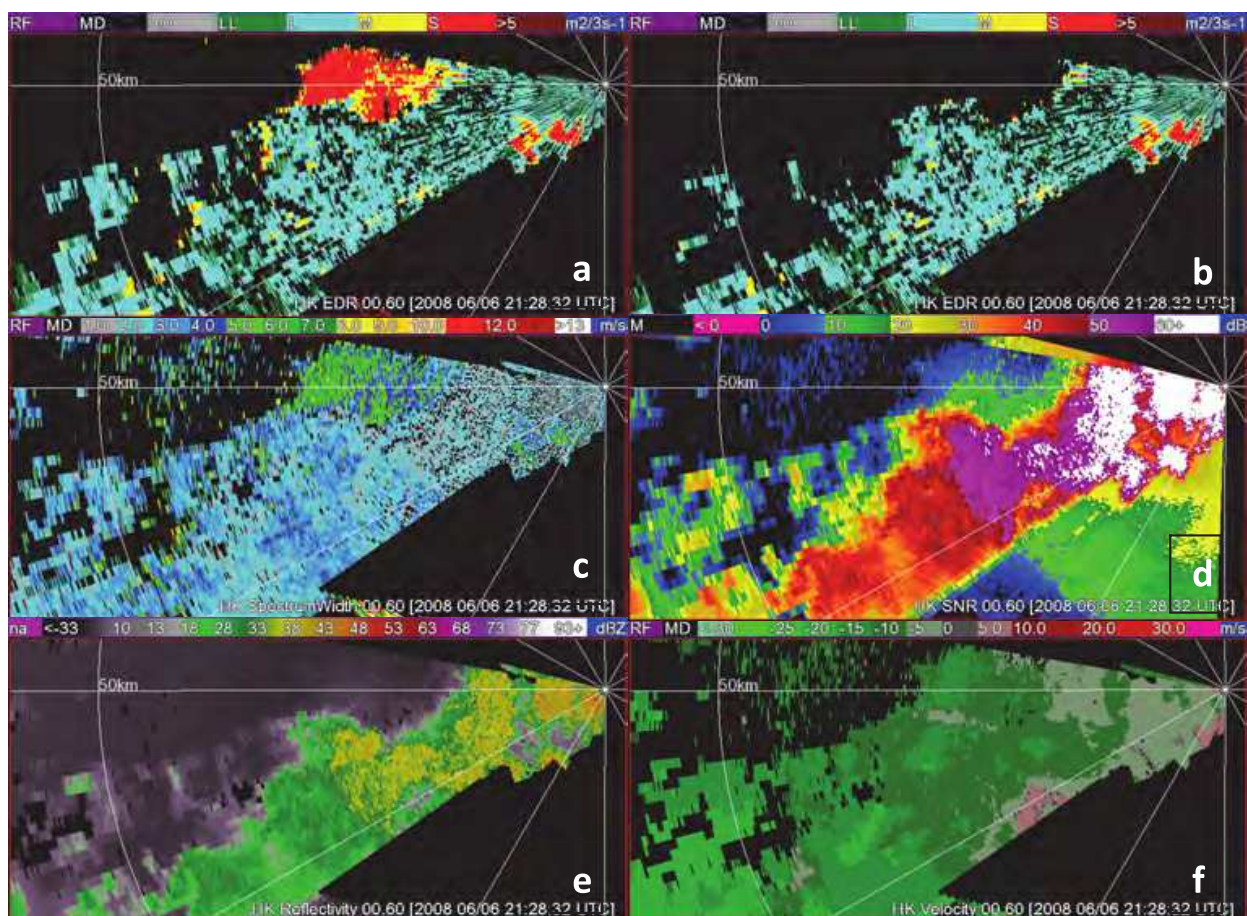


Fig. 9. (a) EDR, (b) EDR with SNR > 20 dB, (c) spectrum width, (d) SNR, (e) reflectivity, and (f) Doppler velocity at elevation angle of  $0.6^\circ$  at 21:28 UTC on 6 June 2008. Range ring is 50 km and azimuths are every  $30^\circ$ .



On the other hand, there are two small regions near the radar at the range of 6 km where EDR is also high. But in this region there is relatively strong horizontal shear of the radial wind component (Figure 9(f); green color identifies the wind has a component toward the radar and red color indicates wind is away from the radar). Furthermore, the reflectivity is about 10 dBZ and SNR is around 35 dB. Because this region is on the downwind side of Lantau Island, the ambient flow (green in Figure 9(f)) is blocked by the Island and back flow (red in Figure 9(f)) is induced. The wind shear contributions, computed using Eq. (8), have been removed from the calculation EDR presented in Figure 9(a). Thus the EDR should not be biased by strong shear of mean radial wind. Thunderstorm outflow may be another reason for the severe turbulence in this region. Because there is no strong horizontal shear of the Doppler velocity field in the region 270° and 25 km, we conclude that the large EDRs presented in that region of Figure 9(a) are unrealistic. After a threshold  $\text{SNR} > 20$  dB is applied, it can be seen that these large EDR values are removed (Figure 9(b)).

Using the Hong Kong TDWR observations in 2006 and 2008, many EDR maps were produced and examined. Here wind shear contribution has been removed from spectrum width measurements. Here the mean wind shears in horizontal and vertical directions are calculated by using mean radial velocity field smoothed by a 9 points median filter along the radar beam in the Eq.(8). Figure 10 shows two typical EDR maps during light rain at 21:32 UTC on 27 April 2006 (Figure 10(a)) and during a thunderstorm at 13:17 UTC on 13 June 2008 (Figure 10(b)). For most of the scanned area, EDR is low and turbulence is classified as insignificant or light (green and light blue). Small pockets of moderate and severe turbulence (yellow and red) are scattered in the scanned area. Near the Lantau Island, moderate and severe levels of turbulence are frequently observed in the cases we studied. The blockage of the Island on the ambient flow may be a reason for the occurrence of the turbulent airflow. Based on the numerical simulations, Clark et al. (1997) and Chan (2009) found that mechanical effect of a mountainous island is a source of the generation of the turbulence.

Clear air cases have been investigated as well, but we found that SNR of the Hong Kong TDWR is too low to provide reliable and meaningful EDR maps.

After the EDR maps were generated, EDR profiles along the flight paths can be compared with aircraft measured EDR. A total of 14 cases are selected to make the comparison. The aircraft EDRs are estimated based on the vertical wind measured by aircraft (Cornman et al., 2004).

Radar derived EDR profile is constructed by selecting the EDR in a resolution volume  $V_6$  closest to the flight path and at an elevation angle of 0.6°. There are still differences in the measurement heights between the aircraft and the radar beam for these two EDR datasets. Only a part of the flight path is covered by the radar beam. For example, aircraft approaching runway 25RA is in the radar beam only at the distance between 0.5 and 1.5 nm from the end of runway. From this point of view, EDRs estimated by aircraft and the radar would be compared within this distance interval. It should also be mentioned that radar estimated EDR is based on the spectrum width of the Doppler velocity, i.e. velocity in the radial direction along a radar beam. On the other hand, the aircraft estimated EDR is based on the vertical wind. As such, the two EDR datasets are derived from different components of the wind. Put aside errors in measurement, in order to have agreement turbulence must be isotropic.

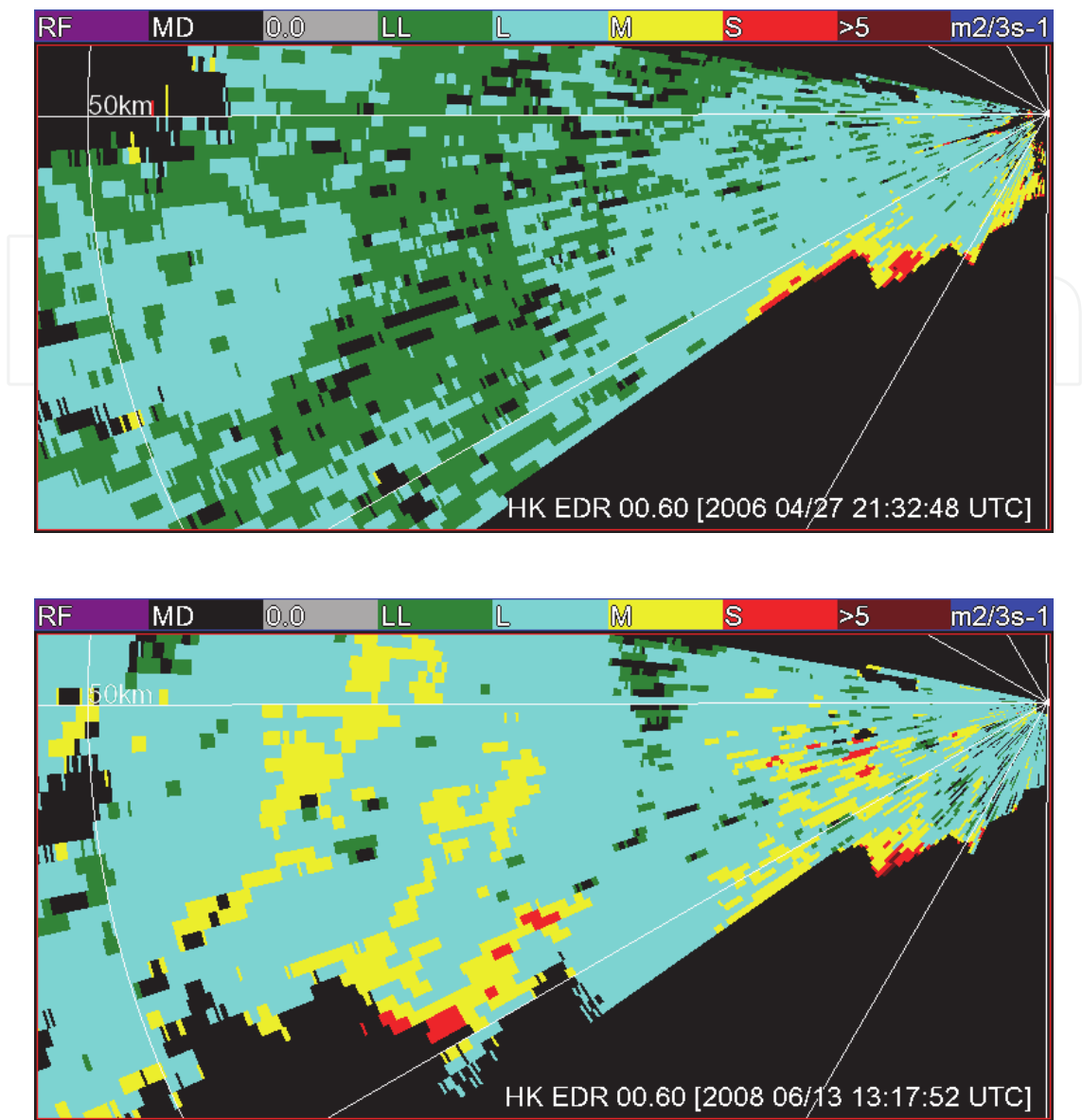


Fig. 10. EDR maps (a) at 21:32 UTC on 27 April 2006 and (b) 13:17 UTC on 13 June 2008. The mountainous Lantau Island is located to the south of the radar scans.

Another issue of the comparison is the contribution of mean wind shear to the measured spectrum width. For the estimation of EDR, the contribution of wind shear has to be extracted from the radar measured spectrum width. But for the comparison with aircraft measured EDR or even turbulence alert for aviation safety, wind shear might not need to be removed. For example if the aircraft experiences a sharp change in altitude, this may not be caused by isotropic turbulence but it is a measure of aircraft response to vertical shear of mean wind. As such, the aircraft estimated EDR based on vertical velocity may be slightly higher. Pilots and passengers in aircraft may also experience severe “turbulence”, which is a combination of the effects of both turbulence and wind shear.

Scatterplots of median and maximum EDR along the 5 nm of flight paths estimated by aircraft and radar are shown in Figure 11. Two plots for each are shown; one in which mean wind shear contributions to the observed spectrum widths are removed and a second plot in

which mean wind shear contribution has been retained. All median EDRs are smaller than  $0.4\text{ m}^{2/3} / \text{s}$  (i.e., moderate or light turbulence). 13 of 14 median EDRs indicate turbulences are light. Based on maximum EDRs, two severe turbulent patches ( $\text{EDR} > 0.5\text{ m}^{2/3} / \text{s}$ ) are detected by both aircraft and radar with wind shear, but they are not on the same flight paths. With wind shear contribution, median and maximum radar EDRs evidently increase.

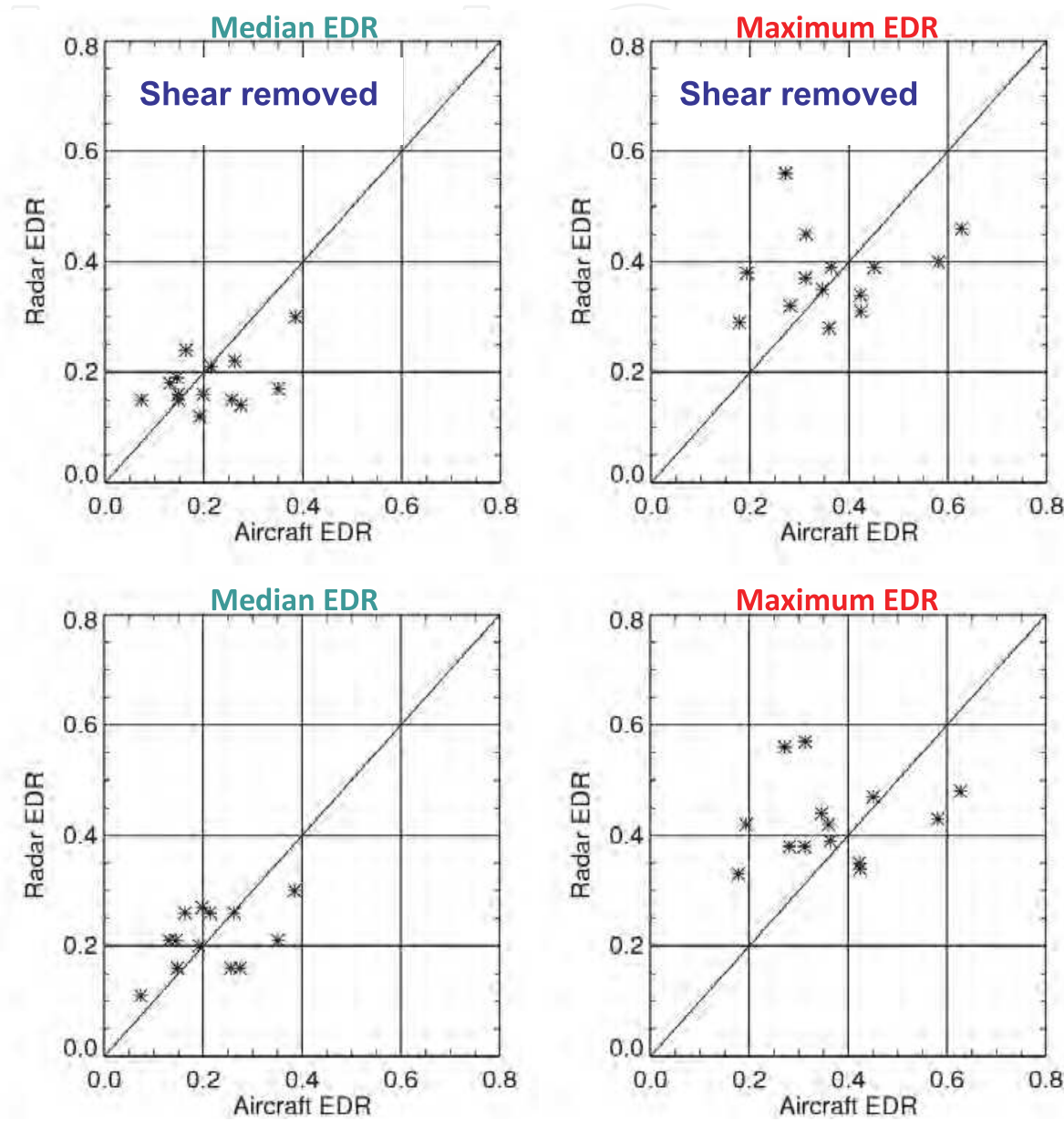


Fig. 11. Scatterplots of median and maximum EDR estimated by aircraft and radar along the 5 nm of flight paths for the selected 14 cases.

Comparing maximum intensity between aircraft and radar without wind shear, 8 of the 14 cases are in the same category. Seven of them are moderate turbulence. For 4 aircraft estimated light turbulence cases, the radar tends to overestimate them as moderate (3 cases) and severe (1 case) with wind shear contribution. After closer examination of the overestimation case at 07:17 UTC on 25 June 2008, it is found that the maximum severe



turbulence only occurs at one radar gate at the distance of 0 nm, closest to the end of the runway. It is noted that at this location, the radar beam is higher than the flight path by about 160m.

We have also compared aircraft and radar estimated EDR profiles including wind shear contribution along the aircraft flight path. For this case, aircraft B777 flew through a storm with maximum reflectivity of 42 dBZ and landed in clouds and light rain at HKIA.

Figure 12 shows the EDR estimated by aircraft and the radar along the flight path 25RA around 13:05 UTC on 19 April 2008. It is one of the two cases in which severe turbulence was encountered by the aircraft. Blue dots in Figure 13 represent the EDR estimated by the aircraft as it was landing at HKIA. Three peaks over  $0.5 \text{ m}^{2/3}/\text{s}$ , classified as severe turbulence, are recorded at distance of 0.77, 3.65, and 4.90 nm away from the runway end. EDR profiles estimated by using radar data at an elevation angle of  $0.6^\circ$  with the wind shear contribution included in the volume scans around 13:05 UTC are overlaid onto the aircraft estimated EDR in Figure 13. The radar estimated EDR profiles at 13:01, 13:05, and 13:09 UTC (brown dots, red squares, and green dots in Figure 13) matches well with aircraft EDR between distance of 0.5 and 1.5 nm, shaded in green color in Figure 13, where the aircraft was in a region common to the  $0.6^\circ$  radar beam. It means that radar and aircraft were measuring turbulence in approximately the same region at nearly the same time.

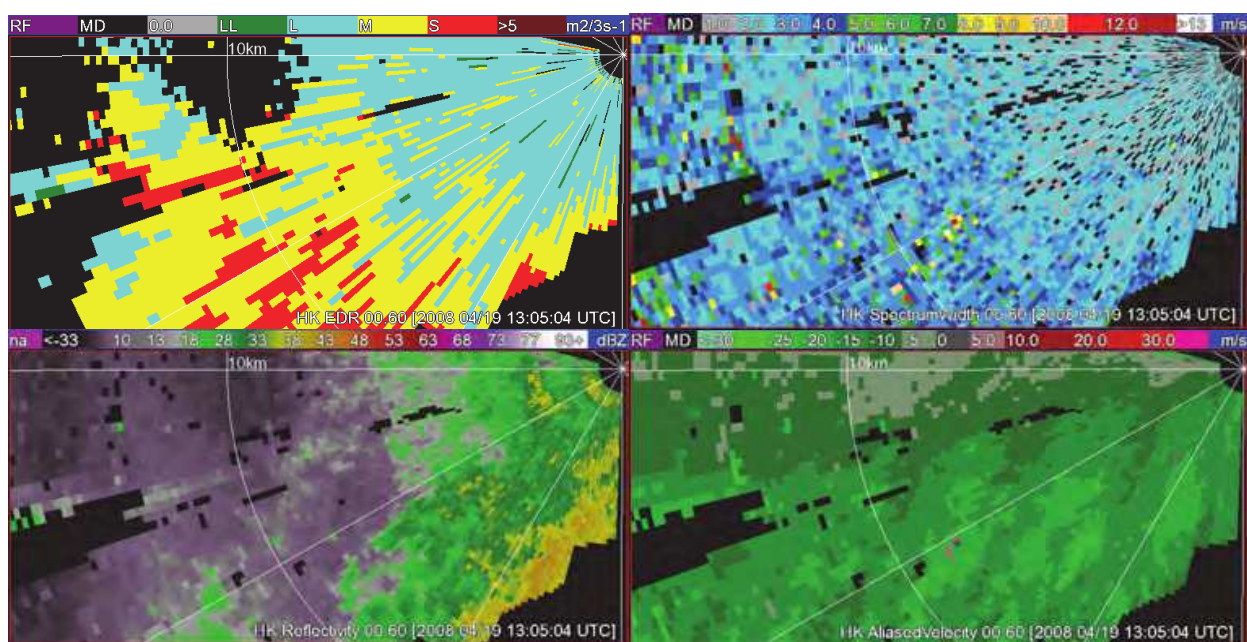


Fig. 12. (a) EDR, (b) spectrum width, (c) reflectivity factor, and (d) Doppler velocity at elevation angle of  $0.6^\circ$  at 13:05 UTC on 19 April 2008. Range ring is at 10 km.

The peaks of these 3 EDR profiles at 13:01, 13:05, and 13:09 UTC are in the green shaded interval and the maximum value is  $0.48 \text{ m}^{2/3}/\text{s}$ , just slightly smaller than  $0.5 \text{ m}^{2/3}/\text{s}$ . In order to find if there are higher EDR near the flight time (13:05 UTC), we examined the EDR for the two scans one minute before and after the passage of the aircraft at 13:05 UTC in the same volume scan at 13:05 UTC. The profiles are shown with light and dark purple dots in Figure 13. High EDRs with values of 0.69 and  $0.76 \text{ m}^{2/3}/\text{s}$  are found within the shaded

interval. This convinces us that the EDR peak is not caused by random error of radar measurements.

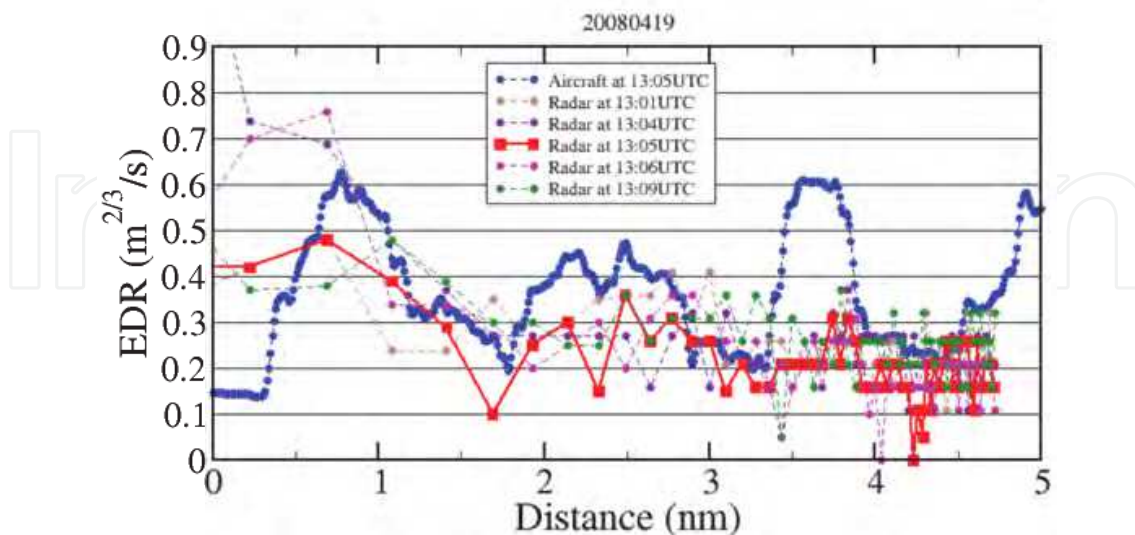


Fig. 13. EDR along the flight path estimated by the aircraft B777 (blue dots) at 13:05 UTC and by the TDWR radar at the time indicated in the legend on 19 April 2008. X axis is the distance between aircraft and the end of runway. The distance interval shaded by the green color indicates where the aircraft passes through the altitude interval observed with the 0.6° elevated beam.

It raises another question: the aircraft may contaminate the radar measurements of the atmospheric status, since the aircraft disturbs the atmosphere and changes the original atmospheric condition in the measurement region as it flies by. In addition, aircraft itself as a target embedded in other scatterers, such as raindrops, may contaminate the spectrum width measurements as well. Both of the two factors could affect spectrum width and EDR value.

It could also be seen that the radar EDR profiles do not match the two aircraft estimated EDR peaks at the distance of 3.65 and 4.90 nm. It might be caused by the spatial difference between the aircraft and the radar beams. The flight heights at the distance of 3.65 and 4.90 nm are higher than the radar beams by about 260 m and 400 m respectively.

Wind shear contribution to spectrum width measurement for this case has been examined. After removing wind shear contribution, the EDR peak at the distance of 0.69 nm is reduced from 0.48 to 0.46  $m^{2/3}/s$  (not shown) at 13:05 UTC. It means that wind shear contribution is small in this region. Because wind shear of the large scale mean wind should be persistent over the 4 minute for entire volume scan, the EDR peaks without wind shear contribution at 13:04 and 13:06 UTC at the distance of 0.69 nm are reduced to 0.67 and 0.74  $m^{2/3}/s$  respectively. It indicates severe turbulence that is matched with aircraft estimate at 13:05 UTC.

Note that the aircraft estimated EDR is considered as ground truth in the above analysis, but it also contains errors and requires significant QC effort, especially as airplane is climbing or descending (Gilbert et al., 2004).

## 5. Conclusion

This chapter discusses the aviation applications of TDWR. This radar issues microburst alerts which are crucial in the assurance of aviation safety. A typical case of microburst detection by TDWR in association with intense thunderstorms is described first in this chapter. Then the applications of TDWR in the alerting of windshear and turbulence are described. Windshear is alerted through the calculation of windshear hazard factor, which is a rather well established technology. On the other hand, the use of spectrum width data from the radar in the alerting of turbulence has a relatively shorter development history, and the technology is under exploration in Hong Kong.

Study is underway in Hong Kong to use X-band radar in the alerting of windshear and turbulence on experimental basis at the Hong Kong International Airport. The use of long-range S band radar in the alerting of turbulence for enroute aircraft is also under study. Such progress of these studies would be reported in the future.

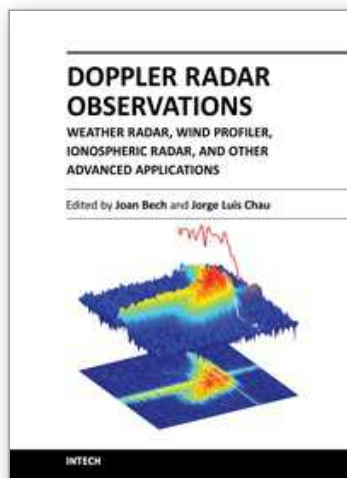
## 6. References

- Brewster, K.A. and D.S. Zrnica, 1986: Comparison of eddy dissipation rate from spatial spectra of Doppler velocities and Doppler spectrum widths. *J. Atmos. Oceanic Technol.*, 3, 440-452.
- Chan, P.W., 2009: Atmospheric turbulence in complex terrain: verifying numerical model results with observations by remote-sensing instruments. *Meteorology and Atmospheric Physics*, 103, 145-157.
- Clark, T.L., T. Keller, J. Coen, P. Neill, H. Hsu, and W.D. Hall, 1997: Terrain-induced turbulence over Lantau Island: 7 June 1994 Tropical Storm Russ case study. *J. Atmos. Sci.*, 54, 1795-1814.
- Cornman, L. B., G. Meymaris, and M. Limber, 2004: An update on the FAA Aviation Weather Research Program's in situ turbulence measurement and reporting system. Preprints, Eleventh Conf. on Aviation, Range, and Aerospace Meteorology, Hyannis, MA, Amer. Meteor. Soc., P4.3.
- Doviak, R. J., and D. S. Zrnica, 2006: Doppler radar and weather observations. Dover Publications Inc., Mineola, New York, 562 pp. (except for the preface with links to online errata and supplements, this is an exact copy of the 1st and 2nd printing of the 1993 Academic Press edition).
- Fang, M., R.J. Doviak, and Melnikov, 2004: Spectrum width measured by the WSR-88D radar: Error sources and statistics of various weather phenomena. *J. Atmos. Oceanic Technol.*, 21, 888-904.
- Gilbert, D., L.B. Cornman, A.R. Rodi, R.G. Frechlich, and R.K. Goodrich, 2004: Calculating EDR from aircraft wind data during flight in and out of Juneau AK: Techniques and challenges associated with non-straight and level flight patterns. Preprints, 11th Conf. on Aviation, Range and Aerospace Meteorology. Hyannis, MA, Amer. Meteor. Soc., CD-ROM, 4.4.
- Haverdings, H., 2000: Updated specification of the WINDGRAD algorithm, NLR TR-2000-63, National Aerospace Laboratory, 2000.



- Hinton, D.A., 1993: Airborne derivation of microburst alerts from ground-based Terminal Doppler Weather Radar information – a flight evaluation, NASA Technical Memorandum 108990, NASA.
- Labitt, M., 1981: Coordinated radar and aircraft observations of turbulence. Project Rep. ATC 108, MIT, Lincoln Lab, 39 pp.
- Lee O.S.M. 2004. 'Enhancement of the Anemometer-based System for Windshear Detection at the Hong Kong International Airport.' Eighth Meeting of the Communications/Navigation/Surveillance and Meteorology Sub-Group (CNS/MET/SG/8) of APANPIRG, Bangkok, Thailand, 12 - 16 July 2004. International Civil Aviation Organization.
- Merritt, M.W., 1987: Automated detection of microburst windshear for Terminal Doppler Weather Radar, presented at SPIE Conference on Digital Image Processing and Visual Communications Technologies in Meteorology, 27-28 October 1987, Cambridge, MA, USA.
- Proctor, F.H., D.A. Hinton and R.L. Bowles, 2000: A windshear hazard index, presented at 9th Conference on Aviation, Range, and Aerospace Meteorology, 11-15 September 2000, Orlando, FL., USA.
- Shun C.M. and Chan P.W. 2008. Applications of an infrared Doppler Lidar in detection of wind shear. *Journal of Atmospheric and Oceanic Technology* 25: 637-655.

IntechOpen



## **Doppler Radar Observations - Weather Radar, Wind Profiler, Ionospheric Radar, and Other Advanced Applications**

Edited by Dr. Joan Bech

ISBN 978-953-51-0496-4

Hard cover, 470 pages

**Publisher** InTech

**Published online** 05, April, 2012

**Published in print edition** April, 2012

Doppler radar systems have been instrumental to improve our understanding and monitoring capabilities of phenomena taking place in the low, middle, and upper atmosphere. Weather radars, wind profilers, and incoherent and coherent scatter radars implementing Doppler techniques are now used routinely both in research and operational applications by scientists and practitioners. This book brings together a collection of eighteen essays by international leading authors devoted to different applications of ground based Doppler radars. Topics covered include, among others, severe weather surveillance, precipitation estimation and nowcasting, wind and turbulence retrievals, ionospheric radar and volcanological applications of Doppler radar. The book is ideally suited for graduate students looking for an introduction to the field or professionals intending to refresh or update their knowledge on Doppler radar applications.

### **How to reference**

In order to correctly reference this scholarly work, feel free to copy and paste the following:

P.W. Chan and Pengfei Zhang (2012). Aviation Applications of Doppler Radars in the Alerting of Windshear And Turbulence, Doppler Radar Observations - Weather Radar, Wind Profiler, Ionospheric Radar, and Other Advanced Applications, Dr. Joan Bech (Ed.), ISBN: 978-953-51-0496-4, InTech, Available from: <http://www.intechopen.com/books/doppler-radar-observations-weather-radar-wind-profiler-ionospheric-radar-and-other-advanced-applications/aviation-applications-of-doppler-radars-in-the-alerting-of-windshear-and-turbulence>

**INTech**  
open science | open minds

### **InTech Europe**

University Campus STeP Ri  
Slavka Krautzeka 83/A  
51000 Rijeka, Croatia  
Phone: +385 (51) 770 447  
Fax: +385 (51) 686 166  
[www.intechopen.com](http://www.intechopen.com)

### **InTech China**

Unit 405, Office Block, Hotel Equatorial Shanghai  
No.65, Yan An Road (West), Shanghai, 200040, China  
中国上海市延安西路65号上海国际贵都大饭店办公楼405单元  
Phone: +86-21-62489820  
Fax: +86-21-62489821

© 2012 The Author(s). Licensee IntechOpen. This is an open access article distributed under the terms of the [Creative Commons Attribution 3.0 License](https://creativecommons.org/licenses/by/3.0/), which permits unrestricted use, distribution, and reproduction in any medium, provided the original work is properly cited.

IntechOpen

IntechOpen